

Cite this: *J. Mater. Chem. A*, 2023, **11**, 11222

Electrolyte-mediated assembly of graphene-based supercapacitors using adsorbed ionic liquid/non-ionic surfactant complexes†

Sima Lashkari,^{ab} Manila Ozhukil Valappil,^{ID} ^{ab} Rajinder Pal^a and Michael A. Pope^{ID} ^{*ab}

Supercapacitors are increasingly being used in energy management systems due to their ability to operate efficiently at high power densities. To boost supercapacitor performance, high surface area electronically conducting materials like graphene in combination with room temperature ionic liquids are a promising combination capable of increasing cell voltage and specific capacitance, respectively – requirements for higher energy density. To overcome challenges associated with graphene aggregation and restacking, we present an electrolyte-mediated, electrode fabrication strategy where a commonly used ionic liquid (IL) is complexed with a non-ionic surfactant to design a surface active spacer that adsorbs to the surface of reduced graphene oxide in dispersion and acts as the electrolyte in the final consolidated electrode composite. We find a general trend that the gravimetric capacitance scales linearly with surfactant plus IL content reaching values as high as 243.8 F g⁻¹ at 5 mV s⁻¹ after which the electrodes are not solid enough to process. While this is amongst the highest reported for IL-based supercapacitors, the maximum in volumetric capacitance (80 F cm⁻³) is achieved at intermediate spacer fractions due to challenges associated with achieving fully dense composites.

Received 17th February 2023
Accepted 3rd May 2023

DOI: 10.1039/d3ta00959a

rsc.li/materials-a

1. Introduction

Electrochemical double layer capacitors (EDLCs), also known as supercapacitors, store energy at the double layer of closely spaced ionic and electronic charge formed at a high surface area electrode/electrolyte interface upon the application of a potential.^{1,2} Due to the fast and reversible nature of this phenomena, EDLCs can safely deliver high power and long cycle life, which makes them attractive candidates for critical, high power applications.² Nevertheless, EDLCs fall short of delivering high energy density. Most commercially available EDLCs can deliver around 5 to 8 W h L⁻¹³ which is significantly less than incumbent technologies such as lead acid batteries (50–90 W h L⁻¹)⁴ and Li-ion batteries (490–650 W h L⁻¹).⁵

The volumetric energy density (E_V) of an EDLC can be estimated as $E_V \propto C_V U^2$ where C_V is the volumetric capacitance of a single electrode and U is the maximum operating voltage of the device. The volumetric capacitance of a single electrode can be found as $C_V = \rho_{\text{bulk}} C_G$ where C_G and ρ_{bulk} are the gravimetric capacitance of a single electrode and the bulk density of the electrode, respectively. Therefore, researchers seek to find an

optimal C_G , U and ρ_{bulk} in order to maximize E_V . The gravimetric capacitance of the electrode is the product of its areal double layer capacitance (C_{DL}) and its specific surface area (SSA). Thus, materials with intrinsically high C_{DL} and high ion accessible surface area are needed. While graphene, which possesses a high theoretical surface area of 2675 m² g⁻¹, is widely referred in the literature as an ideal candidate for EDLC, its low quantum capacitance reduces its potential for supercapacitor application. Reduced graphene oxide (rGO) with more defects and functional groups has a higher quantum capacitance.⁶ However, its surface area is often severely compromised by aggregation and restacking of individual sheets when assembled into a dense electrode.^{7–9}

Several techniques have been proposed so far for improving the SSA of rGO such as using a physical spacer,^{10–12} chemical activation,^{13,14} creating crumpled or curved rGO,^{15,16} and using the electrolyte as spacer.^{17–21} Among these methods, electrolyte-mediated electrode fabrication has shown significant promise, enabling some of the highest reported C_V , since it can deliver a high ρ_{bulk} . However, this method often imposes processing challenges.¹⁷ For example, Yang *et al.*¹⁷ used the repulsive forces between solvated rGO as a spacer during vacuum filtration. The solvent, initially water, was replaced with an ionic liquid (IL) electrolyte by solvent exchange, delivering C_V values of up to 209 F cm⁻³. Introducing an IL has the advantage of significantly boosting device energy density due to their large electrochemical voltage window (4–5 V) compared to aqueous or organic electrolytes.²² Vacuum filtration produces graphene-

^aDepartment of Chemical Engineering, University of Waterloo, 200 University Avenue, Waterloo, ON, N2L 3G1, Canada. E-mail: michael.pope@uwaterloo.ca

^bWaterloo Institute for Nanotechnology, University of Waterloo, 200 University Avenue, Waterloo, ON, N2L 3G1, Canada

† Electronic supplementary information (ESI) available. See DOI: <https://doi.org/10.1039/d3ta00959a>

based electrodes with a high degree of alignment, and thus high ρ_{bulk} (e.g., up to 1.2 g cm^{-3}) has been reported. However, this value is reported before the electrolyte imbibition step, which likely reduces the density further.¹⁷ Nevertheless, this process is inherently slow due to the self-limiting aspects of filter-cake formation and thus, not amenable to roll-to-roll processing. To overcome this limitation, Pope *et al.*¹⁹ used evaporative consolidation to create a gel mixture of graphene oxide (GO) and hydrophilic IL (1-ethyl-3-methylimidazolium tetrafluoroborate) which was later heat treated to reduce the GO. This method provided a high C_G of 140 F g^{-1} but yielded a mediocre C_V of 65 F cm^{-3} since the IL does not adsorb directly on the surface of GO resulting in an inhomogeneous distribution of electrolyte and a lower bulk density of 0.46 g cm^{-3} . To improve upon this method, She *et al.*²⁰ used a common non-ionic surfactant (Tween 20) and the hydrophobic IL, 1-ethyl-3-methylimidazolium bis(trifluoromethanesulfonyl)imide (EMImTFSI), to form stable colloidal assemblies in aqueous solution which were shown to spontaneously adsorb on the surface of GO and act as a spacer in the final dry composite. They later removed the surfactant by heat treatment, which also partially reduced the GO giving rise to a high bulk density of 0.76 g cm^{-3} and large C_V of 218 F cm^{-3} which remains one of the highest reported for a graphene-based composite. Although this method has improved both C_V and C_G , due to the presence of IL in the composite electrode, the heat treatment temperature was constrained, leaving behind remaining functional groups which could possibly improve the capacitance but adversely affected the cycle life performance of the device. Additionally, heat treating the GO/IL composite on aluminum current collectors was not possible due to corrosion, necessitating the use of heavier copper current collectors which were also discolored after heat treatment. More recently, this method was adopted by Fan *et al.*²¹ for MXenes, which have inherently high electrical conductivity (*i.e.*, no reduction is required), eliminating the heat treatment step but leaving behind the surfactant in the electrolyte.

Expanding on this approach, we demonstrated recently that mixing several non-ionic surfactants such as Triton X-100 and Pluronic P123 can, in addition to imparting surface activity to a non-surface active IL,^{23,24} have a beneficial effect on the C_{DL} measured at the IL/glassy carbon interface. Despite adding these uncharged and effectively electrochemically inert surfactants to the IL, a significant increase in C_{DL} is observed; for example, over 100% improvement is observed at 40 wt% P123.²⁴ This was discussed to be a result of the reduction in ionic correlations within the IL by PEO chain of the non-ionic surfactants.²⁵

These works motivated us to explore how the P123 surfactant system, which is known to be a good dispersant for rGO, might be leveraged alone or complexed with the IL, EMImTFSI, as a spacer requiring no additional processing steps after electrode casting onto an aluminum current collector. We show that using either P123 alone or various IL/P123 compositions leads to composite electrodes with a continuously tunable gravimetric capacitance which simply depends on how much spacer material is added to the composite. Composites exhibiting

maximal gravimetric and volumetric capacitance are evaluated and demonstrate promising performance as high voltage, symmetric supercapacitors.

2. Experimental method

2.1 Preparation of GO

GO was synthesized using Tour's modified Hummer's method.²⁶ Briefly, 360 mL sulfuric acid, 40 mL of phosphoric acid and 18 g of potassium permanganate were mixed in a three-neck, round bottom flask placed within an ice bath. 3 g of graphite flakes (Alfa Aesar, 99.9% purity, -10 mesh) were added slowly to the mixture and mixed to ensure a sufficient dispersion of all the ingredients. The flask was then heated overnight at 47°C . After 16 h, the resulting thick purple slurry was added slowly to ice water (around 200 mL) and stirred using a glass rod. The unreacted potassium permanganate was reduced by the dropwise addition of H_2O_2 to the dispersion, which changed the dispersion color from brownish/purple to bright yellow. The resulting GO was washed twice with 10% hydrochloric acid and 4 times with ethanol by centrifugation using Fisher Scientific accuSpin3 at 3000 rpm for 30 min. Then, the pellet was dispersed in DI water and dialyzed for ~ 7 days until the pH of the dispersion was ~ 4 .

2.2 Preparation of reduced graphene oxide (rGO)

The graphene oxide was chemically reduced using hydrazine reduction method by Stankovich *et al.*²⁷ To a round bottom flask, 50 mL of 2 mg mL^{-1} GO dispersion in water was added and 200 μL hydrazine hydrate (35 wt%) was added to the dispersion (based on the ratio hydrazine : GO of 7 : 10 wt/wt as described by Li *et al.*).²⁸ This ratio was found to effectively remove 99% of the oxygen functional groups.²⁹ The dispersion was left overnight at 98°C . The color of the initially yellowish gold GO dispersion turned black. The resulting rGO was then filtered and washed with 500 mL of DI water. The filter cake was collected (care was taken not to let the filter cake dry out which can lead to irreversible aggregation and restacking) and was subsequently used to make electrodes. Using this method, the GO was found to lose roughly 60% of its original weight. To make this estimate, around 100 mg of GO was reduced using the above-mentioned method and then filtered and air-dried overnight. The resulting greyish black powder was placed in a vacuum oven (no heating) for two days to remove any remaining moisture and then was weighed. This procedure was repeated three times.

2.3 Preparation of rGO/P123/IL composite electrode

For the preparation of the electrode, we added 5% of a commercially available reduced graphene oxide (Angstrom Materials Inc.) as a conductive additive which was mixed with the lab-prepared rGO collected from the hydrazine reduction and added to an aqueous dispersion of P123 at a concentration of 0.2 mg mL^{-1} . The amount of P123 was varied to achieve 10 to 80 wt% of P123 (on a dry basis) to the dispersion. The dispersion was tip ultrasonicated for 30 min at 60% amplitude using

a Sonics Vibra-cell unit. Then, EMImTFSI was added to the dispersion and ultrasonicated for another 30 min. The ratio of IL to P123 was varied between 1, 2 and 3. The final dispersion was sprayed into liquid nitrogen using a spray bottle to flash freeze the IL/surfactant adsorbed layer onto the surface of the rGO.²³ The resulting frozen slurry was collected and freeze dried to produce a composite powder of mixed rGO/P123/IL (flash freeze drying). At lower concentration of P123 and IL, a flocculent powder was collected. However, with increasing the concentration of both P123 and IL, this powder further clumped together, giving rise to a paste like material at around 80 wt% P123, as a result of excess polymer. This powder was pressed onto a carbon coated aluminum current collector (single carbon layer, Landt instruments) using a 1/2-inch pellet pressing die (MTI corp.) and force of 5 tons (metric) at different mass loadings.

2.4 Electrochemical characterization of two electrode cell using rGO/P123/IL composite electrodes

Symmetric, two electrode cells were made by sandwiching a glass fiber separator soaked with 100 μL of EMImTFSI between two rGO/P123/IL composite electrodes in a stainless steel two-electrode split test cell (TMAX Battery Equipment). The cell assembly was performed in an argon-filled glovebox (less than 1 ppm O_2 and H_2O). The two electrode cells were characterized by cyclic voltammetry (CV), galvanostatic charge discharge (GCD) and electrochemical impedance spectroscopy (EIS) using a BioLogic SP-300 potentiostat. The single electrode gravimetric capacitance, C_G , was calculated based on GCD and CV using eqn (1) and (2), respectively.

$$C_G = \frac{2i}{m_{\text{active}}(U - U_{\text{drop}})/\Delta t} \quad (1)$$

$$C_G = \frac{2I_{\text{ave}}}{m_{\text{active}}\nu} \quad (2)$$

where i is the current set for the GCD test, m_{active} is the mass of active material on one electrode, U is device operating voltage (3 V), U_{drop} is the voltage drop at the beginning of the discharge cycle and Δt corresponds to the time it takes for the cell to fully discharge. I_{ave} is the averaged current at the 1.5 V point on CV curve and ν is the scan rate. And the volumetric (C_V) and areal capacitance (C_A) are calculated as:

$$C_V = \rho_{\text{bulk}} C_G \quad (3)$$

$$C_A = \rho_A C_G \quad (4)$$

The bulk density (ρ_{bulk}) was calculated by dividing the active electrode materials by the product of electrode thickness and the area of the electrode. The electrode thicknesses were measured using a caliper. To counter the effect of minor surface irregularities, the average of four thicknesses is reported. The areal density (ρ_A) was calculated by dividing the mass of active electrode material by the area of electrode.

The full cell volumetric energy density and power density were calculated using the following relations:

$$E_v = \frac{1}{8}\rho_{\text{bulk}} C_G U^2 \quad (5)$$

$$P_v = \frac{E_v}{\Delta t} \quad (6)$$

where Δt is the discharge time.

The gravimetric energy density, E_G is calculated using the following eqn (7):

$$E_G = \frac{1}{8}C_G U^2 \quad (7)$$

Importantly, this calculation in eqn (7) excludes the weight contribution of device components other than the active electrode material.

2.5 Characterization

Scanning electron micrographs (SEM) were taken on a field-emission scanning electron microscope (Zeiss UltraPlus) with an acceleration voltage of 10 kV. Energy dispersive X-ray spectroscopy (EDS, EDAX Apollo X) was performed on a thick pressed pellet of the sample using an acceleration voltage of 20 kV under 500 \times magnifications. The data were collected over three different regions on each sample.

Electrical conductivity of rGO was measured using a four-point probe station (Ossila). The samples were made by grinding rGO in a mortar and pestle and pressing them using a hydraulic press into a 0.4 mm thick pellet.

Fourier Transform Infrared Spectroscopy (FTIR) of rGO and GO were performed using NEXUS 670. For GO, a thin film was created by drop casting and air-drying diluted GO dispersions on an aluminum weighing boat, the free-standing GO film was then placed between two slits and subsequently placed into the sample holder for testing. The rGO samples were made by mixing rGO power with KBr 1 : 100 ratio (rGO to KBr) in mortar and pestle and then pressed in hydraulic press into a thin disc. Using 32 number of scans and a resolution of 4 in IR transmittance mode, the data were collected in the range of 4000–400 cm^{-1} wavenumber.

Fluorescence spectroscopy was performed for the characterization of IL adsorption using a Varian Carry Eclipse with an excitation wavelength of 550 nm. The resulting emission was collected between 560–600 nm. The adsorption study was performed using a method reported in our previous study.²³ Briefly, EMImTFSI was labeled using Rhodamine B (Rh B) dye and was added to the aqueous dispersion of P123 ($C_{\text{P123}} = 0.4 \text{ mg mL}^{-1}$) using ultrasonication to make different weight ratios of P123/IL = 1, 2, and 3. The emission spectra were collected for the resulting dispersions and set as control. A fixed amount of rGO was added to the P123 dispersions to make the concentration of 0.2 mg mL^{-1} and sonicated for 30 min. IL at different ratios was then added and sonicated for another 30 min. The final dispersion was centrifuged using Eppendorf centrifuge 5424 at 15 000 rpm for 10 min and the supernatant was tested under the same excitation as control samples and the emission spectra were collected and compared with that of the control samples

for each IL/P123 ratio. For each IL/P123 ratio, the sensitivity of the device was set to max out the signal from control emission wavelength, for better visual contrast, and the subsequent supernatant spectra were collected using the same device sensitivity.

X-Ray diffraction was performed using a MiniFlex II unit (Rigaku Americas, Cu K α radiation) from $2\theta = 6$ to 50° using a scan width of 0.05° and a scan speed of 1° min^{-1} . For testing GO, the aqueous GO dispersion was drop-cast onto a glass slide and air-dried. It was then used directly for testing, and for rGO, a thick pellet was made and placed on the sample holder for testing. Care was taken to match the thickness of the pellet with the depth of the cavity of the sample holder to avoid shifting the diffraction angles.

Dynamic light scattering (DLS) was performed using a Zetasizer nano 90, Malvern. Samples were prepared by first dispersing the surfactant in water and then adding a fixed amount of EMImTFSI and further dispersion by

ultrasonication. The final dispersion was filtered using a syringe filter with $0.2 \mu\text{m}$ pore size.

3. Results and discussion

3.1 Characterization of IL adsorption on rGO

The adsorption of IL onto the rGO surface was verified using fluorescence spectroscopy as shown in Fig. 1. When the Rh-B labeled IL is added to the rGO/P123 dispersion, the dark colored dispersion remains stable (Fig. 1a) but can be separated from the supernatant by centrifugation (Fig. 1c). The fluorescence spectra of a control IL/P123 = 1, with no rGO, and the supernatant of the same samples after adsorption onto rGO (unadsorbed IL/Rh B/P123 complex) are depicted in Fig. 1b. The significant drop in the intensities suggests that most of the IL is bound to the rGO with only a small amount remaining free in solution. From the depleted IL, the adsorbed amount (in mg IL/mg rGO) is estimated as shown in Fig. 1d. These amounts are

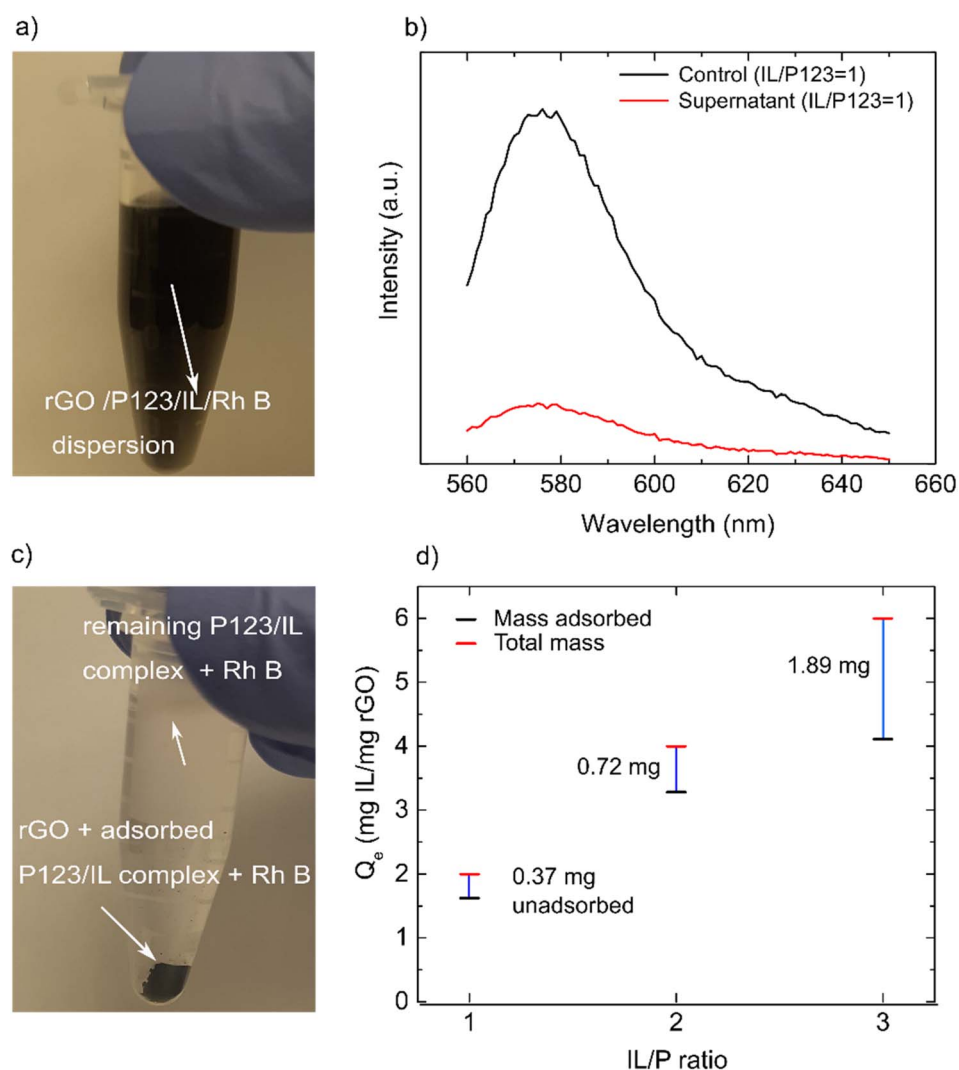


Fig. 1 Characterization of adsorption P123/IL complex on rGO: (a) photograph of dispersion of rGO/P123/IL, (b) comparison of the emission spectra from supernatant dispersion and control dispersion (*i.e.*, without rGO) for IL/P123 = 1, (c) photograph of rGO pellet with adsorbed P123/IL complex, (d) adsorbed amount in comparison to total IL mass added for each IL/P123 ratio on rGO. The difference is the free concentration.

larger than the adsorbed amounts that we previously reported for similar IL/non-ionic surfactant (Tween 20 and Triton X-100) systems adsorbed to GO prior to reduction (*i.e.*, $Q_{\max} \sim 1\text{--}3$ mg IL/mg depending on concentration).²³ According to studies performed on the adsorption of Pluronic (P123 and F127) on GO surfaces, these two surfactants interact with the hydrophobic section of GO using their PPO chain.^{30,31} Since rGO is expected to have a larger proportion of more hydrophobic graphene domains compared to GO, it can more efficiently adsorb the surfactant, and therefore, the mixed adsorbate (P123/IL complex).

The concentration of surfactant in all dispersions is below the critical micelle concentration (cmc) of P123 which is ~ 1.7 mg mL⁻¹ or 0.313 mM.³² Based on this, we expect the surfactant molecules to be dissolved as discrete monomers in the bulk solution which are in equilibrium with an adsorbed phase. As we add IL, interactions between IL molecules and surfactant lead to the delivery of IL to the surface. These interactions have been observed between imidazolium protons and the PEO chain of Pluronic triblock copolymers. However, PPO chains remained intact as the ether oxygen in PPO is shielded by methyl groups.^{33,34} In addition, P123 was reported to break the cation-anion interactions in imidazolium ILs by forming stable

cation/P123 and anion/P123 interactions.³⁴ Therefore, one likely explanation is that IL molecules are being delivered to the rGO surface by complexation with the PEO chains of P123 while PPO groups bond to the rGO surface using hydrophobic interactions.^{30,31}

From Fig. 1d, the percentage of unadsorbed molecules are 18%, 18%, and 31% for IL/P123 ratio of 1, 2 and 3, respectively. Therefore, when we have up to twice the IL to P123 in the dispersion, we get higher adsorption, implying that each surfactant can carry two IL molecules to the surface. Interestingly, when studying these colloidal dispersions at a concentration above the cmc, we see a similar trend, that P123 complexes with the IL, forming mixed micelles for IL/P123 mass ratio of 2 or less (ESI, Fig. S1c†). Increasing the amount of IL led to swelling of micelles and formation of IL aggregates. Such behavior has been observed in the literature for Pluronic and imidazolium-based ILs.³⁵

3.2 Characterization of GO and rGO

The as-prepared GO exhibits a C/O ratio of 1.43 ± 0.02 (by atomic ratio) measured by EDS analysis of the samples, which is increased to 10.3 ± 0.2 after hydrazine reduction, in line with

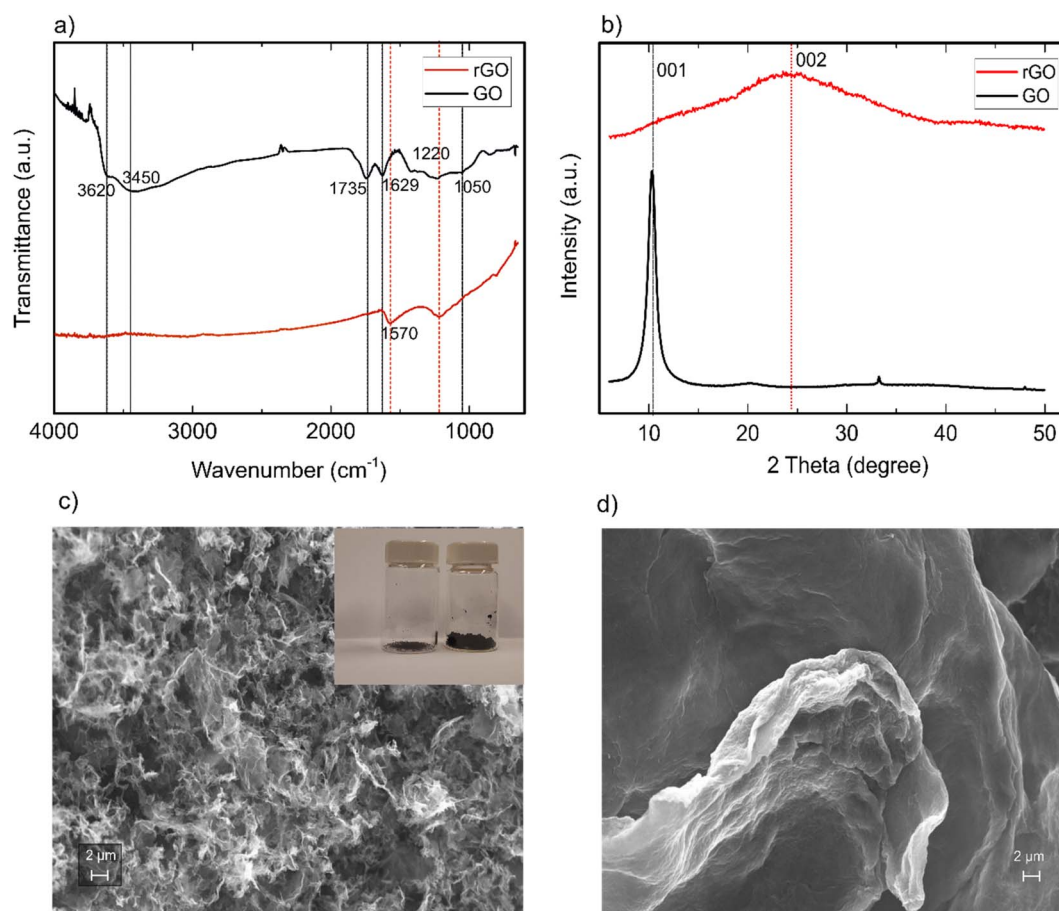


Fig. 2 Characterization of rGO and GO: (a) FTIR spectra of rGO (black) and GO (red), (b) XRD patterns of rGO (black) and GO (red), (c) SEM image of flash-freeze dried rGO. Inset shows the comparison in volume between the same amount of evaporatively dried (left)- and flash freeze-dried (right) samples, (d) SEM image of evaporatively dried rGO.

similar values reported in the literature.²⁷ The conductivity of the rGO was found to be $\sim 400 \text{ S m}^{-1}$ and also similar to previous reports.²⁷ To make a comparison between the functional groups present in both GO and rGO, their spectra were compared using FTIR. Fig. 2a shows the spectra of GO (black) and rGO (red). The O–H stretching of free hydroxyl groups absorb in the 3620 cm^{-1} ($3700\text{--}3584 \text{ cm}^{-1}$). The O–H stretching vibration of water molecules can be found at a lower frequency of 3420 cm^{-1} ($3550\text{--}3200 \text{ cm}^{-1}$). The C–O stretching vibrations are found at $1260\text{--}1000 \text{ cm}^{-1}$. The peak at 1050 cm^{-1} can be assigned to epoxy group (C–O–C), while the peak at 1220 cm^{-1} can be allocated to hydroxyl groups (C–OH). The C=C stretching is observed at 1629 cm^{-1} and the carbonyl and carboxylic group (C=O) appears at around 1735 cm^{-1} ($1740\text{--}1720 \text{ cm}^{-1}$).³⁶

The rGO shows two distinguished bands near 1220 cm^{-1} and 1570 cm^{-1} which can be assigned to C–OH groups²⁹ and C=C stretching absorption band,³⁷ respectively. By comparison of these two spectra, considerable amounts of functional groups such as carbonyl, carboxyl, and epoxy have been eliminated using the hydrazine reduction method, and the amount of sp^2 hybridized carbon has been enhanced causing the material to transition from electrically insulating to electronically conducting.

Fig. 2b shows the XRD profiles for both GO and rGO. For GO, a sharp peak at 10.5° originating from the 001 plane, corresponds to an average interlayer spacing of $\sim 0.84 \text{ nm}$ due to the presence of oxygen-containing functional groups. In contrast, the XRD pattern of rGO exhibits a broad reflection at 24° (002 plane). This shift is due to the reduction in interlayer spacing to 0.37 nm as a result of losing the functional groups and

restacking of the rGO sheets to a spacing closer to that of graphite (0.34 nm).

Fig. 2c and d compare the SEM images of rGO obtained using two different drying techniques, the flash freeze drying (Fig. 2c) and the air-drying method (Fig. 2d). The Inset in Fig. 2c compares the volumes of ($\sim 6 \text{ mg}$) air-dried sample (leftmost figure) to the flash freeze dried sample (rightmost figure), which demonstrates the larger volume (or reduced bulk density). As it can be seen from the SEM images (Fig. 2b and c), the freeze dried rGO consists of individual rGO sheet that are curved and wrinkled. However, evaporatively dried samples show clumps of rGO and is hard to identify the individual sheets. Freeze drying of rGO therefore, provides a significantly reduced bulk density, which is expected to lead to a higher surface area³⁸ compared to that of evaporatively dried rGO.^{10,39}

3.3 Electrochemical performance of rGO/P123/IL composite electrodes

The gravimetric capacitance of a series of rGO electrodes prepared with or without the IL/surfactant complexes is shown in Fig. 5. The capacitance of rGO that was evaporatively dried (*i.e.*, air-dried), had a capacitance of only 62.8 F g^{-1} . Samples by which aggregation had been minimized by spray-freeze drying increased the capacitance to 95.4 F g^{-1} , an $\sim 51\%$ enhancement. Interestingly, these electrodes had a similar bulk density after pressing into electrodes which demonstrates the known severe sensitivity of graphene or rGO ion-accessible surface area on processing conditions with each material being the same rGO but just assembled in a different way. Incorporating P123 into the dispersion improved the capacitance further to 168 F g^{-1}

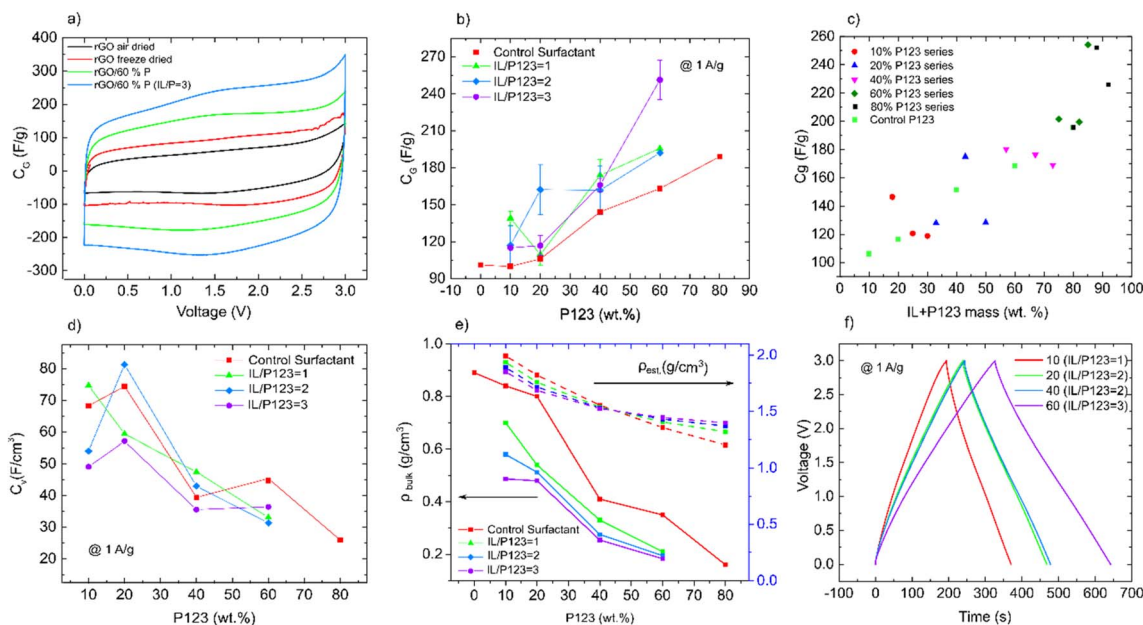


Fig. 3 Electrochemical performance of rGO/P123/IL composite electrodes at various concentrations of surfactant and IL, with electrode loading 1 mg cm^{-2} (a) CV of rGO control (freeze-dried and air-dried), rGO/P123 (at 60 wt% P123) and rGO/P123/IL (at 60 wt% P123) (IL/P = 3), scan rate = 5 mV s^{-1} , (b) C_g of electrodes vs. surfactant wt% at 1 A g^{-1} , (c) C_g of electrodes vs. total added spacer mass%, (d) C_g of electrodes vs. surfactant wt% at 1 A g^{-1} , (e) density comparison of the electrodes, ρ_{est} denotes density estimated assuming a linear combination of individual component densities vs. measured bulk density (ρ_{bulk}), (f) GCD comparison of best performing electrodes at 1 A g^{-1} .

(an additional 76% improvement), while, using the IL/P123 surfactant complex boosted the capacitance an additional 45% to 243.7 F g^{-1} . Adding the P123 or P123/IL complex as a spacer provides a significant boost in capacitance while retaining a pseudo-rectangular CV up to 3 V.

In Fig. 3b, we study the effect of P123 wt% on the achievable capacitance by galvanostatic charge–discharge testing (Fig. 3b). However, since P123 is not ionically conducting, the test cell was assembled under flooded IL conditions and mutual diffusion of P123 and IL are expected to take place. This time-dependent process was observed as the capacitance of the cell (area of the CV plot), increased from the first cycle to the last cycle (10^{th}), indicating that more rGO surface area became ion-accessible with time (ESI, Fig. S2a†). While this worked to improve the capacitance, instead, including the IL with the P123 as part of the adsorbed layer complex, had a stronger effect on boosting capacitive performance (Fig. 3b) while the electrolyte work-in cycles were found unnecessary (Fig. S2b†). This indicated that there was already enough IL in the composite to sustain ionic contact to all rGO surface area. It is interesting to note the maximum capacitance for 10 wt% P123 electrode series occurs as IL/P = 1, while for the 20 wt% P123 series, the maximum gravimetric capacitance of 160 F g^{-1} was reached at IL/P123 = 2, for the sake of brevity, we will refer to it as 20% P (2), and adding extra IL resulted in a drop in capacitance. Similar phenomena can be observed for the 40 wt% P123 series. However, for the 60 wt% P123 series, the maximum capacitance occurs at the IL/P123 = 3 (or 60% P (3)) which is also the largest capacitance among all the tested series ($C_G = 243.7 \text{ F g}^{-1}$). One likely explanation for this behavior is the possible effect of free, dissolved or emulsified IL on the self-assembly of P123/IL and the kinetics of adsorption.^{40,41} Therefore, certain ratios of IL/P123, at various concentrations of surfactant, result in more uniform coverage of the surface, as it was shown that this uniform coverage is critical to achieving large capacitance.²⁰ For 80 wt% P123, the addition of IL made the rheological properties of the powder unsuitable for pressing into a semi-solid electrode disc. Therefore, we have not reported any values for this electrode as it could not be easily cast onto a current collector for capacitance measurements.

However, regardless of the peculiar behavior of C_G with respect to IL/P123 ratio, considering the total mass added to the composites, the capacitance is generally continuously increasing (Fig. 3c) in a nearly linear fashion with the total mass of spacer material used, suggesting that a synergic effect of both P123 and IL as spacer. Nevertheless, increasing the amount of spacer has an adverse effect on the C_V of our electrodes as less of the electrode volume is active material with a larger proportion being spacer (Fig. 3d). Fig. 3d compares the volumetric capacitance of the whole series of composite electrodes. The maximum C_V is 80 F cm^{-3} and occurs at 20% P (2) with C_G of 160 F g^{-1} . The second-best performance in terms of C_V can be assigned to 10% P (1) electrodes with volumetric capacitance of 75 F cm^{-3} . However, for 60% P(3) electrodes with the highest C_G , the C_V drops to 45 F cm^{-3} . This drop is due to a decrease in electrode density as a result of air entrapment during electrode processing which creates voids in the film. Furthermore, the

wrinkled structure of freeze-dried rGO (as depicted in Fig. 2c) also reduces the density of the electrodes where the sheets are not as aligned as those deposited by something like vacuum filtration.¹⁷ Fig. 3e compares the experimental bulk density (ρ_{bulk}) vs. the estimated density of a fully dense composite assuming the composite density is a linear combination of the densities of the pure components (ρ_{est}). For 60% P(3) electrode, the estimated density of a fully dense composite is $\sim 1.4 \text{ g cm}^{-3}$. If we were able to achieve this while retaining the IL accessible surface area, we would be able to boost the C_V further to 350 F cm^{-3} .

For the best performing electrode of each series, their GCD curves were compared in Fig. 3f at 1 A g^{-1} . The GCD curves are nearly triangular in shape with only a slight voltage drop at the beginning of the discharge cycle ($\sim 0.05 \text{ V}$ for 1 A g^{-1}). This can be ascribed to the purely double layer charging of these composite electrodes after the chemical reduction of GO (see Fig. 2). Our previous attempt using heat treatment of the electrode at a low temperature of $300 \text{ }^\circ\text{C}$ resulted in partial removal of the oxygen containing functional groups which degraded the device cycle-life.²⁰

Further, based on the active material mass/volume we calculated the energy and power densities (both volumetric and gravimetric) of our electrodes of various P123 wt%, at 1 A g^{-1} . The calculated values have been supplemented in Table S1.† Our materials consist of electrolyte and a surfactant acting as inactive components (“dead-weight”). Therefore, it is worthwhile to compare the energy densities with and without the dead weight. Accordingly, the gravimetric energy densities (at 1 A g^{-1}) including and excluding the dead weight are compared as a function of P123 wt% (using the ratio of IL:P123 = 3) in Fig. S3.† It is evident that the gravimetric energy density drops as inactive mass is added, which is also consistent with the trend in volumetric energy densities since the added volume decreases the electrodes' bulk densities. However, as discussed in reference to Fig. 3e, the experimental bulk densities are far below the estimated ones, implying further improvement to the volumetric energy densities is possible. For example, for a 60% P(3) electrode, if we were able to achieve the estimated density of the electrode $\sim 1.4 \text{ g cm}^{-3}$ for a fully dense composite while retaining the ionic liquid-accessible surface area, we would be able to boost the volumetric energy density further to 88 W h L^{-1} at a gravimetric capacitance of 200 F g^{-1} (Fig. S3†).

Fig. S4† shows the relationship between gravimetric energy densities as a function of C_G for various weight percentages of P123 (IL:P123 = 3). The energy densities calculated considering total mass including non-active components are also given for comparison, again validating that gravimetric energy density drops substantially when inactive mass is considered.

To compare the performance of our electrodes with the literature report, we constructed a Ragone plot of our materials superimposed with the literature reports of similar systems (Fig. S5†). A detailed comparison table has also been supplemented (Table S2†). 20% P(2) electrodes show energy density and power density of 27 W h L^{-1} and 0.44 kW L^{-1} , respectively (also refer to Table S1†) when considering only the electrode volume. At a high power density of 8 kW L^{-1} , the energy density

drops to 16 W h L^{-1} . Also, note that most of the literature reports are based on a voltage window $\geq 3 \text{ V}$, which would be difficult to make a one-to-one comparison of performance, since the energy density scales with the square of the voltage window. Nevertheless, the focus of our paper is to demonstrate a new approach, which is to prevent restacking of rGO using surfactant/IL complexes as a spacer. As evident from Table S2,[†] our electrodes (60% P(3), IL:P123 = 3) demonstrate one of the

highest capacitances in terms of $\text{F g}_{\text{active material}}^{-1}$, which suggests that our approach is amongst the best as a spacer. On the other hand, the volumetric capacitance of our electrodes are limited by sub-optimal bulk densities as discussed earlier. For this reason, the 20% P(2) electrode, which has the optimized value for volumetric energy and power densities is chosen for comparison with the literature values, which as can be seen from Table S2[†] is positioned among the middle of the pack.

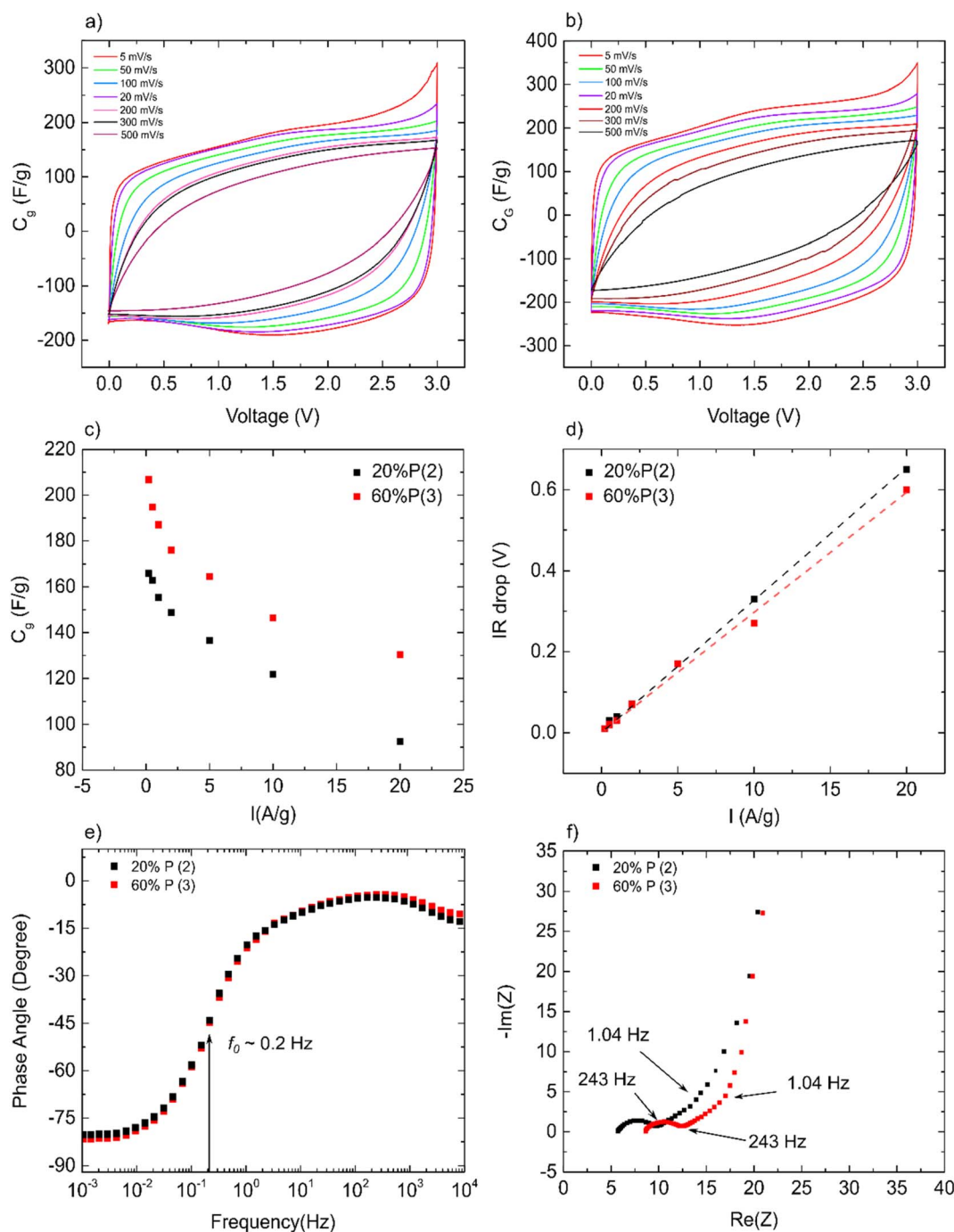


Fig. 4 Comparison between performance of 60% P(3) vs. 20% P(2). (a) CV of 20% P(2), (b) CV of 60% P(3), (c) rate performance for 20% P(2) vs. 60% P(3), (d) IR drop vs. current density comparison for 20% P(2) and 60% P(3), (e) phase angle for 20% P(2) and 60% P(3), (f) EIS comparisons between 20% P(2) and 60% P(3).

While we achieve results consistent with other high-impact literature reports, we do not achieve the highest performance in terms of energy and power densities because of the voltage limitations and the sub-optimal bulk density, and this leads to, not the best, but a competitive performance. Even so, potentially a much higher volumetric energy density is possible with this material if we are able to achieve the estimated bulk density (Fig. S3†).

Comparison of 60% P(3) and 20% P(2) electrode performances

Since 20% P(2) and 60% P(3) electrodes showed the highest volumetric and gravimetric capacitance, respectively, we have carried out a more comprehensive performance assessment in Fig. 4a and b, respectively. The CVs for both electrodes are rectangular in shape and remain so up to a very large scan rate indicating ideal double layer charging. The capacitance *vs.* current densities are compared for both electrodes in Fig. 4c. As can be seen from the plot, both electrodes show good rate performance, maintaining up to $\sim 70\%$ of their original capacitance up to current densities as high as 10 A g^{-1} . This is an indication of both good ionic and electronic conductivity due to the presence of IL/P123 between the rGO. In Fig. 4d, voltage drops (IR drop) *vs.* current density show a linear relationship for both electrodes ($R^2 \sim 0.99$ for both cells), the slope of this line represents the equivalent series resistance (ESR), or internal resistance of the cell,⁴² which reflects the combined resistances due to ion and electron transport.⁴³ The ESR values of 0.032Ω and 0.029Ω were measured for 20% P(2) and 60% P(3), respectively. Fig. 4e shows the phase angle *vs.* frequency for both electrodes. As it can be seen from the plot, the phase angle for both electrodes is close to -90° ($\sim -80^\circ$) at lower frequencies which again signifies ideal double layer capacitance behavior. The frequency at a phase angle of -45° marks the characteristic frequency f_0 where both capacitive and resistive impedances are equal.⁴⁴ This frequency for both of our electrodes is at 0.2 Hz corresponding to a time constant (τ_0) of 5 s . Fig. 4f probes the ion transport properties of both electrodes using EIS. Overall, both electrodes show nearly ideal capacitive behavior judging from the vertical line at the low frequency region. The 45° line from 243 Hz to 1.04 Hz , which is seen for both electrodes, is a result of Warburg-like impedance caused by diffusional resistances at these frequencies.⁴³ Regardless of the larger volume of IL in 60% P(3), both electrodes show the same Warburg-like impedance. However, it should be noted that the 20% P(2) electrodes require initial work-in cycles using a low scan rate of 5 mV s^{-1} while the 60% P(3) did not require this extra step (a comparison between the first scan and the last scan for these two electrodes were made in ESI, Fig. S6†). The semicircle in the high frequency region, which is sometimes referred to as the charge transfer resistance, but for blocking electrodes is more related to the resistance associated with ionic and electronic diffusion processes in the porous electrode, are quite similar and low ($\sim 4 \Omega$).⁴³ These resistances were compared with control samples of 20% P and 60% P (surfactant only) and the rGO only electrode in ESI, Fig. S7.† From Fig. S7a,†

the control sample with rGO as an electrode (no adsorbed IL complex), shows a larger diameter semi-circle ($\sim 9.7 \Omega$) at high frequencies and a more extended Warburg resistance, while with addition of only 20 wt% P123, this resistance reduces to 4.4Ω . The reduction in resistance with only 20 wt% P123 can be related to the enhanced ionic diffusivity facilitated by surfactant spacers, which states the significant role of electrolyte in reducing the overall resistance of the cell. With further increase in the amount of surfactant, the resistance increases ($\sim 6.8 \Omega$) as a result of having excess non-conducting surfactants which also increase the viscosity of the electrolyte. Comparing this value with that of 60% P(3) electrodes, the effect of ordered self-assembly of IL/P123 on the interface prior to electrode assembly can be clearly identified and this effect has already been observed in capacitance enhancement of this electrode (Fig. 3b). The same conclusion can be made from Fig. S7b.†

3.4 Loading study for 20% P(2) electrode

Since 20% P(2) has the highest volumetric capacitance, we have studied its performance at different areal mass loadings of the electrode. Higher loadings are desired as they increase the practical device energy density by increasing the ratio of active material to inactive material (current collectors, membrane separator, *etc.*). By increasing the electrode loading to 1.58 mg cm^{-2} , the gravimetric capacitance stays the same for lower scan rates of 5 mV s^{-1} and 20 mV s^{-1} (20 mV s^{-1} corresponds to 1 A g^{-1}), but drops at higher scan rates losing $\sim 60\%$ of its original values at high scan rate of 500 mV s^{-1} . While at 3.96 mg cm^{-2} loading of active materials, the capacitance drops to 107 F g^{-1} at low scan rate and further reduces to 10 F g^{-1} at 500 mV s^{-1} , losing around 90% of its original capacitance (Fig. 5a). Fig. 5b, compares the GCD curve for different loadings. While for both 0.79 and 1.58 mg cm^{-2} of electrode loading, the GCD stays rectangular with low voltage drop of 0.05 and 0.11 V , respectively, the 3.96 mg cm^{-2} loading electrode shows a much higher voltage drop of 0.29 V which explains the poor rate performance of this electrode. The drop in capacitance at higher loading are usually the result of hindered ionic or/and electronic transport across the electrode cross section. The areal capacitance (C_A) of the electrodes, shown in Fig. 5c, drops at higher mass loading of 3.96 mg cm^{-2} as a result of hindered ionic and/or electronic transport properties.⁴⁵

Performing EDS mapping on the surface of the electrodes shows uniform elemental distribution of O, N, S and F which indicates even distribution of IL throughout the electrode surface (Fig. S8†). A cross sectional view of our electrodes (Fig. S9†), shows the existence of large air gaps, which are the origin of the sub-optimal bulk density and might explain the rise of voltage drop and nonlinear increase in C_A *vs.* loading as a result of broken electronic/ionic percolation. Using the expression for porosity, $P = 1 - \frac{\rho_{\text{bulk}}}{\rho_{\text{est}}}$, and the value of ρ_{bulk} and ρ_{est} from Fig. 3e, the porosity of 20% P(2) is estimated to be around 66% . This porosity is attributed to both electrode processing (using the hydraulic press) and wrinkled structures induced during the freeze-drying process.

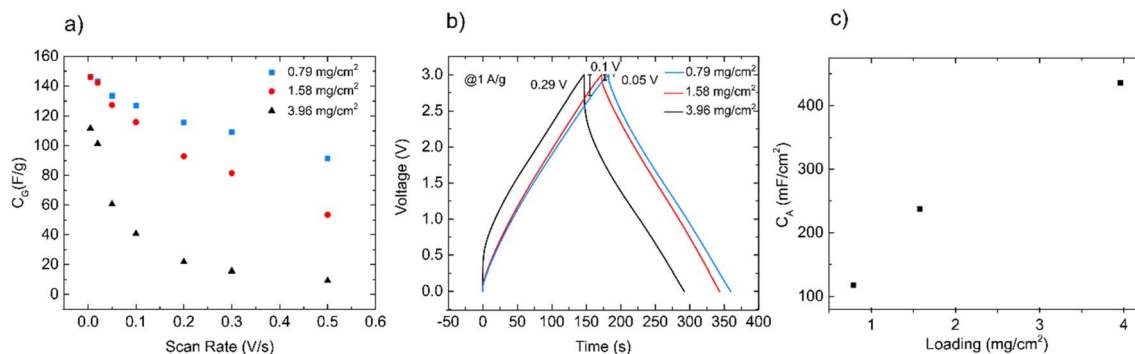


Fig. 5 Loading performance of 20% P(2). (a) Rate performance of electrodes at different loading, (b) GCD comparison of different loading at 1 A g^{-1} , (c) areal capacitance (C_A) as a function of mass loading.

3.5 Cycle life study and comparison of 20% P(2) electrodes to state-of-the-art

The long-term cyclability of our device with 20% P(2) electrode was tested using GCD at 10 A g^{-1} for 10 000 cycles. As depicted by Fig. 6a, the capacitance of the 20% P(2) electrodes increase upon first 1700 cycles up to about 46% of its original capacitance, as a result of work in cycle associated with this electrode (Fig. S6†), and then reduce again at 5000 and 10 000 cycles but retaining around 94% and 80% of its maximum capacitance, respectively. The reduction in capacitance upon long term cycling may be a result of electrolyte decomposition as we are pushing the electrolyte outside of its stability window. The electrochemical stability window (ESW) of EMImTFSI is known to be above 4 V.²⁴ However, interactions between the IL and P123, reduce the oxidative stability of the EMImTFSI and thus reduce the ESW as determined in our previous work.²⁴ Despite this reduced ESW, we could achieve an increase in capacitance implying there is a significantly beneficial effect on the capacitance (an increase by a factor of 88% for P123).²⁴ An investigation of the cell after cycling test revealed discoloration of the electrolyte as a result of this degradation. Further analysis of the voltage window for our supercapacitor was performed using CV at 5 mV s^{-1} and GCD at 0.1 A g^{-1} , which indicates the limits of stability are closer to 2.5 V (Fig. 6b and c). Since we found that the P123 impacts only the oxidative stability of the IL,²⁴ building an asymmetric supercapacitor which traverses a narrower

positive window than negative window is likely to improve the stability in an expanded voltage range.⁴⁶ Preliminary tests on mass balancing (Fig. S10†) indicate that an ESW of $\sim 3.5 \text{ V}$ is possible. However, in future work, we plan to screen other ionic liquids whose stability may be less impacted by the presence of the P123.

Since we have used hydrazine reduced graphene as an active material for our electrode, we first compare our work with Stoller *et al.*³⁹ which also used hydrazine reduced graphene as an active material and PTFE as binder for electrodes combined with organic electrolyte to achieve gravimetric capacity of 99 F g^{-1} . Using our procedure, we increased C_G to more than double the value reported for these materials ($\sim 250 \text{ F g}^{-1}$) indicating the importance of using electrolyte as spacer in improvement of the electrode's SSA. Nevertheless, due to the nature of this reduction method, we still lose considerable surface area of rGO by hydrazine reduction due to instant agglomeration during reduction which cannot be avoided. Other distinguished work can be named as EM-CCG by Yang *et al.*⁸ which yielded C_G of 203.2 F g^{-1} , and C_V of 255.5 F g^{-1} at high electrode density of 1.33 g cm^{-3} using vacuum filtration that enabled flattening of the reduced graphene oxide sheets and imbibition of the electrolyte using capillary forces. However, as it was already mentioned, this method is lengthy and not scalable. Whereas our method based on powder processing is potentially more scalable and economically viable for

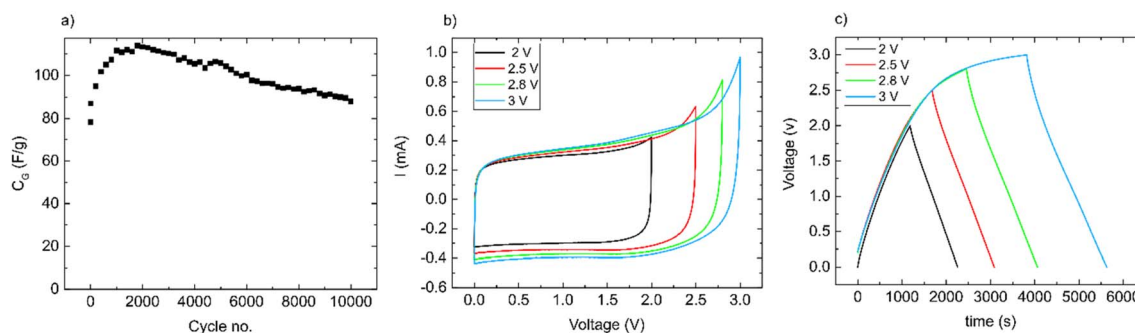


Fig. 6 (a) Cycle stability of 20% P(2) electrode, (b) voltage stability window of electrolyte using 20% P(2) cell, at 5 mV s^{-1} , (c) electrolyte stability window test for cell 20% P(2) at 0.1 A g^{-1} .

fabrication of energy dense electrodes from 2D materials. In addition, with further improvement of the electrode assembly method, we can possibly increase the electrode's bulk density up to $\sim 1 \text{ g cm}^{-3}$ which would result in an increase in volumetric capacitance up to a value of 250 F cm^{-3} . This limitation results from the wrinkled structure of rGO upon reduction and drying which was demonstrated in Fig. 2c. Nevertheless, this method can be applied to other 2D materials which possess good electronic conductivity and high SSA such as MXenes⁴⁷ or the metallic, 1T polymorph of molybdenum disulfide,⁴⁸ where you can achieve ρ_{bulk} closer to the $\rho_{\text{est.}}$ for these new materials and possible enhancement to both C_V and C_G .

The limitations on achieving a larger ESW with this approach would be addressed in a potential future study by screening more ionic liquids whose ESW may not be impacted by P123. In addition, surface active ionic liquids (SAILs) have recently gained recognition as supercapacitor electrolytes due to their unique interaction with electrode and formation of stable structural layers nearby electrified interface.^{49,50} The ions in SAILs can by themselves act as potential surfactants and therefore will not necessitate introducing extra surface-active material such as P123. To alleviate the degradation upon cycling, usage of non-halogenated SAILs will be considered as a non/less-corrosive alternative,⁵¹ as halogenated ionic liquids could corrode the aluminum current collector. We hope that employing these approaches in our future work would help us to overcome the degradation upon charge–discharge cycling as well as maximize the overall performance metrics of our rGO electrodes.

4. Conclusions

In this work, we attempted to address the aggregation of rGO sheets by creating a molecular layer of electrolyte (*i.e.*, EMImTFSI) as spacer on the rGO sheets using the concept of self-assembly of non-ionic surfactants (P123) with the ionic liquid (IL). In this method, the IL molecules are carried to the surface of rGO with the aid of P123, the final dispersion, containing varying P123 concentration and mass ratios of IL to P123, is flash freeze dried. Overall, the C_G increased continuously with an increase in the added spacer mass up to 80 wt% P123. The highest gravimetric capacitance (C_G) of 243.7 F g^{-1} was measured at 60 wt% P123 with IL/P123 = 3 (*i.e.* 60% P(3)), which shows 155% increase in C_G compared to control rGO electrode (freeze dried without the additive, $C_G = 95.4$). While the C_G of the electrode increase linearly with overall addition of spacer materials, measurement of the densities of the electrode shows a continuous drop of the electrode's bulk densities (ρ_{bulk}). Comparing the calculated estimated densities ($\rho_{\text{est.}}$) of the composites with ρ_{bulk} show on average $\sim 66\%$ porosity in the electrodes which may originate from the wrinkled structure of the rGO and air trapped in the rGO/IL/P123 powder during the processing of the electrodes. The volumetric capacitance of the electrodes (C_V) as a result reduces significantly to 45 F cm^{-3} and 75 F cm^{-3} for 20% P(2) and 60% P(3) electrodes, respectively. The overall rate performance of the two electrodes were analogous, the electrodes maintained $\sim 70\%$ of their original

capacitance after 10 fold increase in the current density, while the 60% P(3) did not require an extra work in cycle due to the presence of enough ion conducting molecules in the electrode's composition. For 20% P(2), the cyclic stability test at 10 A g^{-1} shows 94% and 80% capacitance retention up to 5000 and 10 000 cycles, respectively. However, a closer investigation for the electrolyte stability windows reveals the degradation of the electrolyte above 2.5 V. Balancing the electrode's mass can be used to improve the voltage stability window of the device. Overall, this method introduces new prospect for improving the double layer capacitance of 2D materials, with emphasis on materials with inherently high electronic conductivity such as metallic molybdenum disulfide and MXenes.

Conflicts of interest

There are no conflicts to declare.

Acknowledgements

S. L. was supported through the Natural Sciences and Engineering Council of Canada's Discovery Grant program (RGPIN 6600-2015).

References

- 1 P. Simon and Y. Gogotsi, Materials for Electrochemical Capacitors, *Nat. Mater.*, 2008, 7(11), 845–854.
- 2 J. R. Miller and P. Simon, Electrochemical Capacitors for Energy Management, *Science*, 2008, 321(5889), 651–652.
- 3 A. Burke, R&D Considerations for the Performance and Application of Electrochemical Capacitors, *Electrochim. Acta*, 2007, 53(3), 1083–1091.
- 4 *Handbook of Batteries*, ed. Linden, D. and Reddy, T. B., McGraw-Hill handbooks, McGraw-Hill, New York, 3rd edn, 2002.
- 5 J. W. Choi and D. Aurbach, Promise and Reality of Post-Lithium-Ion Batteries with High Energy Densities, *Nat. Rev. Mater.*, 2016, 1(4), 1–16.
- 6 M. A. Pope and I. A. Aksay, Four-Fold Increase in the Intrinsic Capacitance of Graphene through Functionalization and Lattice Disorder, *J. Phys. Chem. C*, 2015, 119(35), 20369–20378.
- 7 J. Xia, F. Chen, J. Li and N. Tao, Measurement of the Quantum Capacitance of Graphene, *Nat. Nanotechnol.*, 2009, 4(8), 505–509.
- 8 H. Ji, X. Zhao, Z. Qiao, J. Jung, Y. Zhu, Y. Lu, L. L. Zhang, A. H. MacDonald and R. S. Ruoff, Capacitance of Carbon-Based Electrical Double-Layer Capacitors, *Nat. Commun.*, 2014, 5(1), 3317.
- 9 F. Bonaccorso, L. Colombo, G. Yu, M. Stoller, V. Tozzini, A. C. Ferrari, R. S. Ruoff and V. Pellegrini, Graphene, Related Two-Dimensional Crystals, and Hybrid Systems for Energy Conversion and Storage, *Science*, 2015, 347(6217), 1246501.

- 10 Y. Si and E. T. Samulski, Exfoliated Graphene Separated by Platinum Nanoparticles, *Chem. Mater.*, 2008, **20**(21), 6792–6797.
- 11 J. Yan, T. Wei, B. Shao, F. Ma, Z. Fan, M. Zhang, C. Zheng, Y. Shang, W. Qian and F. Wei, Electrochemical Properties of Graphene Nanosheet/Carbon Black Composites as Electrodes for Supercapacitors, *Carbon*, 2010, **48**(6), 1731–1737.
- 12 D. T. Pham, T. H. Lee, D. H. Luong, F. Yao, A. Ghosh, V. T. Le, T. H. Kim, B. Li, J. Chang and Y. H. Lee, Carbon Nanotube-Bridged Graphene 3D Building Blocks for Ultrafast Compact Supercapacitors, *ACS Nano*, 2015, **9**(2), 2018–2027.
- 13 Y. Zhu, S. Murali, M. D. Stoller, K. J. Ganesh, W. Cai, P. J. Ferreira, A. Pirkle, R. M. Wallace, K. A. Cychoz, M. Thommes, D. Su, E. A. Stach and R. S. Ruoff, Carbon-Based Supercapacitors Produced by Activation of Graphene, *Science*, 2011, **332**(6037), 1537–1541.
- 14 T. Kim, G. Jung, S. Yoo, K. S. Suh and R. S. Ruoff, Activated Graphene-Based Carbons as Supercapacitor Electrodes with Macro- and Mesopores, *ACS Nano*, 2013, **7**(8), 6899–6905.
- 15 C. Liu, Z. Yu, D. Neff, A. Zhamu and B. Z. Jang, Graphene-Based Supercapacitor with an Ultrahigh Energy Density, *Nano Lett.*, 2010, **10**(12), 4863–4868.
- 16 J. Luo, H. D. Jang and J. Huang, Effect of Sheet Morphology on the Scalability of Graphene-Based Ultracapacitors, *ACS Nano*, 2013, **7**(2), 1464–1471.
- 17 X. Yang, C. Cheng, Y. Wang, L. Qiu and D. Li, Liquid-Mediated Dense Integration of Graphene Materials for Compact Capacitive Energy Storage, *Science*, 2013, **341**(6145), 534–537.
- 18 X. Yang, L. Qiu, C. Cheng, Y. Wu, Z.-F. Ma and D. Li, Ordered Gelation of Chemically Converted Graphene for Next-Generation Electroconductive Hydrogel Films, *Angew. Chem., Int. Ed. Engl.*, 2011, **50**(32), 7325–7328.
- 19 M. A. Pope, S. Korkut, C. Punckt and I. A. Aksay, Supercapacitor Electrodes Produced through Evaporative Consolidation of Graphene Oxide-Water-Ionic Liquid Gels, *J. Electrochem. Soc.*, 2013, **160**(10), A1653–A1660.
- 20 Z. She, D. Ghosh and M. A. Pope, Decorating Graphene Oxide with Ionic Liquid Nanodroplets: An Approach Leading to Energy-Dense, High-Voltage Supercapacitors, *ACS Nano*, 2017, **11**(10), 10077–10087.
- 21 Q. Fan, R. Zhao, M. Yi, P. Qi, C. Chai, H. Ying and J. Hao, Ti₃C₂-MXene Composite Films Functionalized with Polypyrrole and Ionic Liquid-Based Microemulsion Particles for Supercapacitor Applications, *Chem. Eng. J.*, 2022, **428**, 131107.
- 22 M. Shi, S. Kou and X. Yan, Engineering the Electrochemical Capacitive Properties of Graphene Sheets in Ionic-Liquid Electrolytes by Correct Selection of Anions, *ChemSusChem*, 2014, **7**(11), 3053–3062.
- 23 S. Lashkari, M. Chekini, R. Pal and M. A. Pope, Aqueous, Mixed Micelles as a Means of Delivering the Hydrophobic Ionic Liquid EMIM TFSI to Graphene Oxide Surfaces, *Langmuir*, 2022.
- 24 S. Lashkari, R. Pal and M. A. Pope, Ionic Liquid/Non-Ionic Surfactant Mixtures as Versatile, Non-Volatile Electrolytes: Double-Layer Capacitance and Conductivity, *J. Electrochem. Soc.*, 2022, **169**(4), 040513.
- 25 N. C. Osti, K. L. Van Aken, M. W. Thompson, F. Tiet, D. Jiang, P. T. Cummings, Y. Gogotsi and E. Mamontov, Solvent Polarity Governs Ion Interactions and Transport in a Solvated Room-Temperature Ionic Liquid, *J. Phys. Chem. Lett.*, 2017, **8**(1), 167–171.
- 26 D. C. Marcano, D. V. Kosynkin, J. M. Berlin, S. Alexander, Z. Sun, S. Alexander, L. B. Alemany, W. Lu and J. M. Tour, Improved Synthesis of Graphene Oxide - ACS Nano (ACS Publications), *ACS Nano*, 2010, **4**(8), 4806–4814.
- 27 S. Stankovich, D. A. Dikin, R. D. Piner, K. A. Kohlhaas, A. Kleinhammes, Y. Jia, Y. Wu, S. T. Nguyen and R. S. Ruoff, Synthesis of Graphene-Based Nanosheets via Chemical Reduction of Exfoliated Graphite Oxide, *Carbon*, 2007, **45**(7), 1558–1565.
- 28 D. Li, M. B. Müller, S. Gilje, R. B. Kaner and G. G. Wallace, Processable Aqueous Dispersions of Graphene Nanosheets, *Nat. Nanotechnol.*, 2008, **3**(2), 101–105.
- 29 P. Zhu, M. Shen, S. Xiao and D. Zhang, Experimental Study on the Reducibility of Graphene Oxide by Hydrazine Hydrate, *Phys. B*, 2011, **406**(3), 498–502.
- 30 B. J. Hong, O. C. Compton, Z. An, I. Eryazici and S. T. Nguyen, Successful Stabilization of Graphene Oxide in Electrolyte Solutions: Enhancement of Biofunctionalization and Cellular Uptake, *ACS Nano*, 2012, **6**(1), 63–73.
- 31 Y. Yan, L. Piao, S.-H. Kim, W. Li and H. Zhou, Effect of Pluronic Block Copolymers on Aqueous Dispersions of Graphene Oxide, *RSC Adv.*, 2015, **5**(50), 40199–40204.
- 32 P. Alexandridis, J. F. Holzwarth and T. A. Hatton, Micellization of Poly(Ethylene Oxide)-Poly(Propylene Oxide)-Poly(Ethylene Oxide) Triblock Copolymers in Aqueous Solutions: Thermodynamics of Copolymer Association, *Macromolecules*, 1994, **27**(9), 2414–2425.
- 33 D. F. Miranda, T. P. Russell and J. J. Watkins, Ordering in Mixtures of a Triblock Copolymer with a Room Temperature Ionic Liquid, *Macromolecules*, 2010, **43**(24), 10528–10535.
- 34 J.-C. Jiang, S.-C. Li, P.-M. Shih, T.-C. Hung, S.-C. Chang, S. H. Lin and H.-C. Chang, A High-Pressure Infrared Spectroscopic Study on the Interaction of Ionic Liquids with PEO-PPO-PEO Block Copolymers and 1,4-Dioxane, *J. Phys. Chem. B*, 2011, **115**(5), 883–888.
- 35 L. Zheng, C. Guo, J. Wang, X. Liang, S. Chen, J. Ma, B. Yang, Y. Jiang and H. Liu, Effect of Ionic Liquids on the Aggregation Behavior of PEO-PPO-PEO Block Copolymers in Aqueous Solution, *J. Phys. Chem. B*, 2007, **111**(6), 1327–1333.
- 36 *Spectrometric Identification of Organic Compounds 7e by Silverstein.*
- 37 W. Chen, L. Yan and P. R. Bangal, Chemical Reduction of Graphene Oxide to Graphene by Sulfur-Containing Compounds, *J. Phys. Chem. C*, 2010, **114**(47), 19885–19890.
- 38 M. A. Pope, *Electrochemical Double-Layer Capacitors Based on Functionalized Graphene*, Princeton University, 2013.

- 39 M. D. Stoller, S. Park, Y. Zhu, J. An and R. S. Ruoff, Graphene-Based Ultracapacitors, *Nano Lett.*, 2008, **8**(10), 3498–3502.
- 40 B.-Y. Zhu and T. Gu, Surfactant Adsorption at Solid-Liquid Interfaces, *Adv. Colloid Interface Sci.*, 1991, **37**(1), 1–32.
- 41 D. M. Colegate and C. D. Bain, Adsorption Kinetics in Micellar Solutions of Nonionic Surfactants, *Phys. Rev. Lett.*, 2005, **95**(19), 198302.
- 42 M. Nagao, K. Kobayashi, Y. Jin, I. Maruyama and T. Hibino, Ionic Conductive and Photocatalytic Properties of Cementitious Materials: Calcium Silicate Hydrate and Calcium Aluminoferrite, *J. Mater. Chem. A*, 2020, **8**(30), 15157–15166.
- 43 G. Wang, L. Zhang and J. Zhang, A Review of Electrode Materials for Electrochemical Supercapacitors, *Chem. Soc. Rev.*, 2012, **41**(2), 797–828.
- 44 P. L. Taberna, P. Simon and J. F. Fauvarque, Electrochemical Characteristics and Impedance Spectroscopy Studies of Carbon-Carbon Supercapacitors, *J. Electrochem. Soc.*, 2003, **150**(3), A292.
- 45 J.-C. Liu, H. Li, M. Batmunkh, X. Xiao, Y. Sun, Q. Zhao, X. Liu, Z.-H. Huang and T.-Y. Ma, Structural Engineering to Maintain the Superior Capacitance of Molybdenum Oxides at Ultrahigh Mass Loadings, *J. Mater. Chem. A*, 2019, **7**(41), 23941–23948.
- 46 J. H. Chae and G. Z. Chen, 1.9 V Aqueous Carbon–Carbon Supercapacitors with Unequal Electrode Capacitances, *Electrochim. Acta*, 2012, **86**, 248–254.
- 47 C. Zhang (John), B. Anasori, A. Seral-Ascaso, S.-H. Park, N. McEvoy, A. Shmeliov, G. S. Duesberg, J. N. Coleman, Y. Gogotsi and V. Nicolosi, Transparent, Flexible, and Conductive 2D Titanium Carbide (MXene) Films with High Volumetric Capacitance, *Adv. Mater.*, 2017, **29**(36), 1702678.
- 48 M. Acerce, D. Voiry and M. Chhowalla, Metallic 1T Phase MoS₂ Nanosheets as Supercapacitor Electrode Materials, *Nat. Nanotechnol.*, 2015, **10**(4), 313–318.
- 49 X. Mao, P. Brown, C. Červinka, G. Hazell, H. Li, Y. Ren, D. Chen, R. Atkin, J. Eastoe, I. Grillo, A. A. H. Padua, M. F. C. Gomes and T. A. Hatton, Self-Assembled Nanostructures in Ionic Liquids Facilitate Charge Storage at Electrified Interfaces, *Nat. Mater.*, 2019, 1–8.
- 50 P. Jain and O. N. Antzutkin, 2-Ethylhexylsulfate Anion-Based Surface-Active Ionic Liquids (SAILs) as Temperature Persistent Electrolytes for Supercapacitors, *Journal of Ionic Liquids*, 2022, **2**(2), 100034.
- 51 P. Jain and O. N. Antzutkin, Nonhalogenated Surface-Active Ionic Liquid as an Electrolyte for Supercapacitors, *ACS Appl. Energy Mater.*, 2021, **4**(8), 7775–7785.